Energy & Environmental Science

Accepted Manuscript

This article can be cited before page numbers have been issued, to do this please use: K. Zhang, Y. Ji, Q. Wu, S. A. Nabavizadeh, Y. Qi and L. Chen, *Energy Environ. Sci.*, 2025, DOI: 10.1039/D5EE01030F.

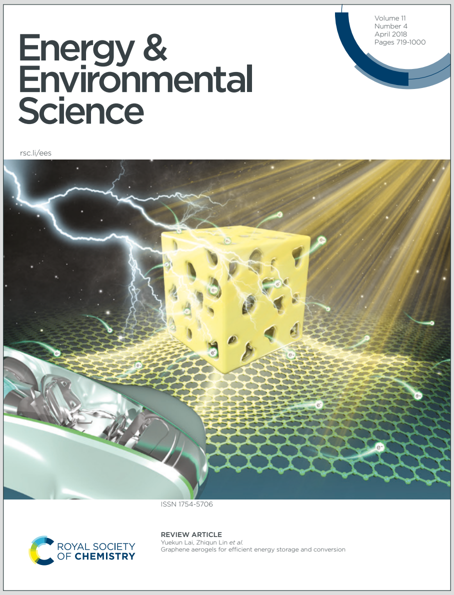

View Article Online
DOI: 10.1039/D5EE01030F

Broader context statement

The solid-electrolyte interphase (SEI) plays a critical role in battery performance and longevity, yet its formation process remains one of the most ambiguous issues in battery science due to the complex, spatially and temporally dynamic nature of this interfacial layer. To capture the rapid SEI formation process across various scales, an atomically informed phase-field model (AI-PFM), capable of handling complex reaction networks with multiple species, is developed. This model enables the investigation of SEI formation and initial growth from nanoseconds to seconds in time and angstroms to 100 nm in length. By tracking the evolution of SEI products and electrolyte species up to surface passivation, the interplay among reaction kinetics, species transport, and electron tunneling during SEI formation is successfully deconvoluted with the governing factors identified. For the first time, this study reveals that the competition between Li-ion diffusion and reaction kinetics is a key determinant of the growth rates of different SEI products. Such deconvolution is difficult to achieve with current modelling and experimental techniques, which underscores the major advancement and benefits of this AI-PFM framework. It offers a unique approach to evaluate the competing complex mechanistic pathways and understand the formation mechanism of SEI.

View Article Online
DOI: 10.1039/D5EE01030F

Simulating solid electrolyte interphase formation spanning 10^8 time scales with atomically informed phase-field model

Kena Zhang[1,+], Yanzhou Ji[1,+,§], Qisheng Wu[2], Seyed Amin Nabavizadeh[1], Yue Qi[2,*] and Long-Qing Chen[1,*]

[1]*Department of Materials Science and Engineering, The Pennsylvania State University, University Park, PA 16802, USA*

[2]*School of Engineering, Brown University, Providence, RI 02912, USA*

Abstract

Solid electrolyte interphase (SEI) dictates the reversibility of advanced electrochemical devices such as batteries, but how it operates with the working ions remains little known. Here, the thickness and compositional evolution of the SEI are tracked over time scales from nanoseconds to seconds by a newly developed atomically informed phase-field multiscale model. We deconvolve the complex interplay among the electron tunneling, species diffusion, and chemical/electrochemical reactions by probing different controlling factors separately and jointly to determine the rate-limiting steps. We reveal the SEI grows beginning with the formation of organic products, followed by the conversion of these organic products into inorganic ones, and in the end the inorganic products fully cover the lithium metal surface to form a passivation layer. While electron tunneling determines the thickness of these layers, the growth rates of the organic and inorganic SEI layers are controlled by the rates of Li-ion diffusion and electrochemical reactions, respectively. This predictive model is universally applicable to multiphase and multicomponent electrochemical systems and represents a significant advancement in simulating complex reaction processes.

*Corresponding Authors: yueqi@brown.edu; lqc3@psu.edu

View Article Online
DOI: 10.1039/D5EE01030F

Key words: lithium batteries, solid electrolyte interphase, multiscale modeling, phase-field modeling, atomistic simulations

View Article Online
DOI: 10.1039/D5EE01030F

Introduction

Solid electrolyte interphase (SEI) plays a vital role in enabling advanced batteries where electrode materials operate beyond the electrochemical stability limits of electrolytes. Its chemical building blocks come from the sacrificial decomposition of electrolytes, which remains conductive to the working ions but prevents electron tunneling that drives the parasitic reactions[1-5]. SEI dictates the reversibility and power density of the battery system. Given such importance, extensive efforts have been devoted to understanding its formation process, but a thorough mechanistic knowledge at a fine timescale is still absent. Recently, it was found that the SEI in Li-ion batteries formed at high charging current during the first cycle extends battery cycle life by an average of 50%[6], revealing that the properties and chemistry of SEI also rely on the rate of formation. Experiments indicated that the initial SEI formation on bare Li metal surface completes in less than 1 second[7]. This rate is comparable to the rate of lithium metal deposition, where a typical 1 mA/cm^2 rate means depositing 8 Li (001) layers or 1.4 nm thick Li atoms in 1 second. Therefore, it is logical to infer that SEI formation and lithium growth compete at the same timescale, resulting in various deposition morphologies[8, 9]. However, experimental limitations in temporal and spatial resolutions often render the challenges to characterize fast *in situ* SEI formation processes and deconvolute the intricate physical and chemical processes across multiple length and time scales.

On the microscopic and mesoscopic timescale, atomic-scale theoretical approaches, such as density functional theory (DFT) calculations and *ab initio* molecular dynamics (AIMD) simulations, offer insights into the reaction energy profiles[10-12], species transport properties[13, 14] and electrolyte reduction pathway within a system[11] that are otherwise unavailable from experiments. However, their simulation time is typically limited to scales of 10 ~ 100 picoseconds

View Article Online
DOI: 10.1039/D5EE01030F

($10^{-11} \sim 10^{-10}$ s) for a system of hundreds of atoms[15, 16], hence proving only limited information on SEI formation, which typically takes up to 1s time scale. A Monte Carlo-molecular dynamics (MC-MD) method can predict the time evolution of SEI species over 10 ns (10^{-8} s) [15]. Using classical reactive force-fields, MD simulations can extend the process further up to 100 nanoseconds (10^{-7} s)[17].

On the macroscopic scale, continuum models have been developed to study the long-term SEI growth over hours and even months[18-23]. Despite the widespread acceptance and observation of two-layer structured SEI in many experimental works, the reaction networks and SEI compositions are simplified so that only single SEI product is included in most continuum-level models[20, 24, 25]. For example, Christensen and Newman[20] proposed a mathematical model to estimate the growth rate of inorganic Li_2CO_3 and calculated that SEI grows around 20 nm in 15 h on graphite, which is limited by the electron transport via Li interstitials diffusion mechanism. The continuum model by Horstmann *et al.* [23] predicted that the capacity fade shifts from a square-root-of-time dependence to a linear time dependence as the charging current density increased, suggesting a shift from diffusion-controlled to electron-migration-controlled SEI growth. Their simulations concluded that it would take several months for an SEI layer of a few nanometers in thickness. While these models have been effective in predicting battery lifetime[25, 26] at macroscale, they overlook several critical kinetic processes involved in SEI growth, which prevents them from accurately predicting the precise composition and morphology of SEI. For instance, the detailed electrolyte reduction reaction networks and the competitive interactions between the various reaction products are neglected. Furthermore, these continuum models fail to account for the electron transport mechanisms, which is crucial for understanding the SEI formation and growth processes.

View Article Online
DOI: 10.1039/D5EE01030F

Since single-scale atomistic simulations are insufficient to capture the complex interfacial reactions and phase transformations involved in SEI formation, multiscale computational frameworks have therefore become indispensable for describing the growth, composition, and dynamic evolution of the SEI and its impact on battery performance. Among these, DFT and MD integrated kinetic Monte Carlo (kMC) methods have been used to track the stochastic reaction nature of electrolyte decomposition. For instance, Gerasimov et al.[27] tracked EC decomposition and SEI formation on Li metal for 100 ns, revealing an inorganic-rich inner layer (LiF/Li_2CO_3) and a porous organic-rich outer layer (Li_2EDC) added up to ~11nm thick. U. Krewer et al.[28] constructed a DFT-kMC-continuum electroneutrality model that predicted a 7-nm-thick inorganic SEI layer within 1 μs (10^{-6} s), while the resulting bilayer architecture (porous Li_2CO_3 beneath dense LiF) deviates from experimental observations[29, 30]. Recently, chemical reaction networks (CRNs) have been developed to automatically identify the reaction pathways for over 80 million reactions among over 5000 species, in which DFT calculations are combined with kinetic Monte Carlo simulations (kMC) to simulate the competition between SEI products within 10 μs (10^{-5} s), revealing the formation of distinct inorganic and organic layers in the SEI[31]. While these kMC-based models have demonstrated success in capturing reaction mechanisms and compositional diversity at the molecular level, they remain limited in temporal and spatial scalability. Their inherently discrete spatial nature restricts the ability to simulate mesoscale structural evolution, such as growth, coarsening, polycrystallinity, and crack formation. Additionally, coupling external physical fields (e.g., mechanical stress relaxation, thermal transport, etc.) into kMC frameworks is generally indirect through modifications of reaction rates.

The phase-field (PF) method offers a continuum framework well-suited for modeling multicomponent, multiphase systems with intrinsic flexibility to incorporate physical fields. By

View Article Online
DOI: 10.1039/D5EE01030F

introducing multiple concentration or order parameter fields governed by free energy functionals, PF models can capture the spatiotemporal evolution of competing SEI phases, while naturally incorporating additional physics such as ion/electron transport, electrochemical reactions, elastic deformation, thermal transport, and other physics effects. Previously, phase-field modeling has already been successfully applied to the investigation of the Li electrodeposition[32-38] and the interaction between Li dendrites and artificial SEIs[39, 40]. However, only a limited number of phase field investigations have been applied to the study the SEI formation and growth[29, 41-43], with several important thermodynamic/kinetic parameters associated with SEI formation being absent. Compared with kMC-based models, previous PF models simplify the SEI as a single homogeneous phase and thus failed to account for the chemical diversity observed experimentally[40, 41]. That is because PF simulations face numerical challenges in simulating multiple moving interfaces with distinct kinetics when tracking the evolution of reaction intermediates, which requires careful parameter calibration and efficient algorithms to ensure numerical stability and convergence.

In this work, we demonstrate that an atomically informed phase-field model (AI-PFM), which incorporates multiple electrochemical reactions, species transport and electrons tunneling process, can track the temporal and spatial evolution of SEI formation from nanoseconds to seconds till it passivates the Li metal surface. The AI-PFM here incorporates these parameters obtained from DFT and MD calculations through simplification and parameterization. We apply this model to a 1-D prototypical battery system with Li metal anode, liquid electrolyte consisting of 1 M $LiPF_6$ in ethylene carbonate (EC), and simulate the evolution of two common SEI products, i.e., organic component dilithium butylene dicarbonate (Li_2BDC) and inorganic component lithium carbonate (Li_2CO_3). By tracking the temporal evolution of the spatial distribution of these products and electrolyte species, we analyze the effect of electron tunneling on SEI thickness,

View Article Online
DOI: 10.1039/D5EE01030F

examine the competition between the reactive and diffusive processes during different SEI products growth, and identify the governing mechanism for the formation of different SEI products. Our findings pinpoint the Li^+ diffusion as the key limiting factor of the formation of organic Li_2BDC during the initial 10^{-5} s scale, whereas Li_2CO_3 directly formed by two-electron reduction of EC is limited by its slow reaction kinetics within around 10^{-2} s. This multiscale approach, for the first time, provides profound insights into the SEI growth across time scales spanning 8 orders of magnitudes (from nanoseconds to seconds) and length scales spanning 3 orders of magnitudes (from angstroms to 100 nm). Furthermore, the model demonstrated the ability of AI-PFM to simulate complex reaction networks that encompass multiphases and multicomponent.

Results and Discussions

Fig. 1 shows the overall framework for modeling the SEI growth integrates multiple electrochemical reactions, species transport, and electron tunneling. DFT calculations are utilized to determine the reaction pathways and their corresponding energy profiles, while MD simulations are employed to obtain the diffusivity of species. Next, phase-field simulations are performed to study the temporal and spatial evolution of SEI products, incorporating parameters derived from atomic-scale calculations. Details of all sub-models can be found in **Experimental**.

View Article Online
DOI: 10.1039/D5EE01030F

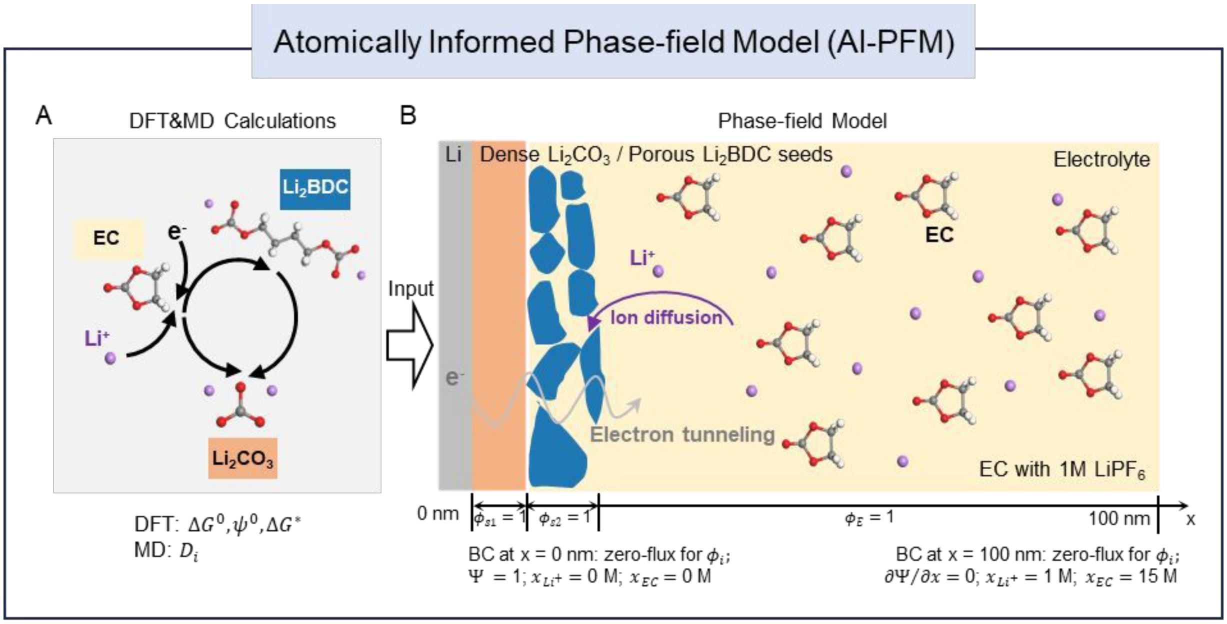

Fig. 1. Schematic modeling framework of SEI formation on lithium metal. (A) Reaction networks and corresponding energy profiles (Gibbs free energy change ΔG^0, reduction potential ψ^0, and kinetic barrier ΔG^* obtained from DFT calculations) of the considered reactions. MD simulations provide the diffusivity of species D_i. (B) Phase-field model and boundary conditions (BC) for three coupled processes: electrochemical reactions, ion diffusion and electron tunneling. The simulation domain ranges from the surface of Li metal electrode at $x = 0$ nm to the bulk liquid electrolyte region (the other boundary is at $x = 100$ nm). The initial concentrations of EC and $LiPF_6$ in the electrolyte are 15 M and 1M, respectively. Unless otherwise specified, the initial SEI nucleus on the Li metal surface consists of two layers: a 0.5 nm dense Li_2CO_3 layer adjacent to the Li metal, and a 6 nm Li_2BDC layer with a porosity of 50% adjacent to the electrolyte. A set of evolving non-conserved order parameters (ϕ_E,ϕ_{S1},ϕ_{S2}) represent the electrolyte, inorganic Li_2CO_3, and organic Li_2BDC phases, respectively.

To obtain the atomic-scale input parameters, we perform an extensive DFT study to establish the predefined reaction network that contains both electrochemical reactions (magenta arrows) and purely chemical reactions (green arrows) (Fig. 2). For each reaction, we calculate its standard Gibbs free energy change ΔG^0 (for purely chemical reactions) or reduction potential ψ^0 (for electrochemical reactions), as well as the electron transfer kinetic barrier ΔG^* according to the Marcus theory [44, 45]. Fig. 2A lists all the reactions considered in our atomistic simulations, involving multiple reactants (Li^+, c-EC, e^-), intermediate species (o-EC^-, Li^+/c-EC, Li^+/o-EC^-,

View Article Online
DOI: 10.1039/D5EE01030F

Li^+/CO_3^{2-}, $2Li^+/o\text{-}EC^-$), and SEI products (Li_2BDC, Li_2CO_3, and C_2H_4). Here, c-EC represents the neutral cyclic EC molecule, and o-EC^- represents the reduced ring-opened EC.

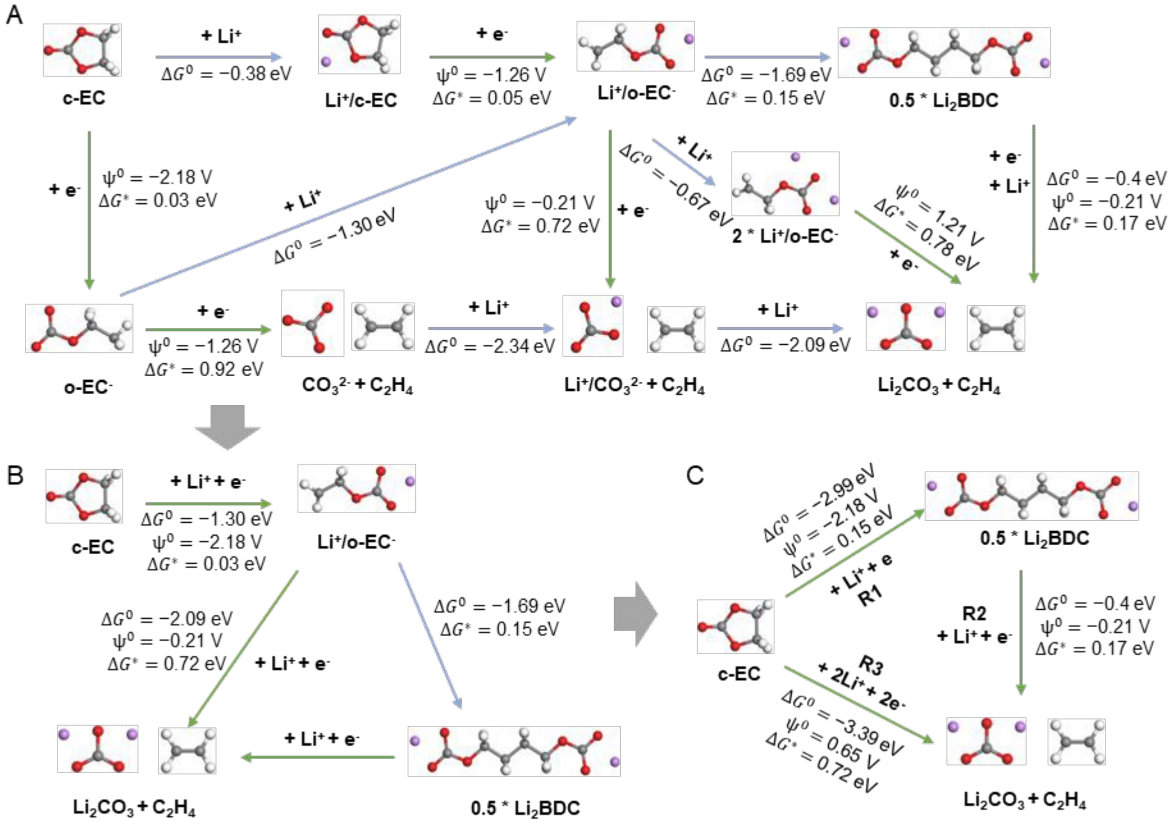

Fig. 2. Illustration of the reaction pathways. (A) All the reaction products and pathways considered in atomistic simulations. The reduction potentials ψ^0 (vs. SHE), the electron transfer kinetic barrier ΔG^* for electrochemical reactions (green arrows), and Gibbs free energy change (ΔG^0) for chemical reactions (blue arrows) are included. (B, C) Simplified reaction pathways and their corresponding thermodynamic and kinetic parameters. The reaction steps, R1, R2, and R3, along with the parameters in (C), are adopted for the phase-field simulations.

While it is possible to develop a comprehensive phase-field model that incorporates all these reactions, such simulations would not efficiently bridge the length and time scales. Thus, we simplify the reaction paths and focus on the primary SEI products: the organic Li_2BDC and inorganic Li_2CO_3 (Fig. 2B and 2C), based on DFT computed thermodynamics driving forces, consist with extensive theoretical and experimental studies[46-48]. We note that Li_2BDC is

View Article Online
DOI: 10.1039/D5EE01030F

thermodynamically more favorable than Li_2EDC, in agreement with other computational studies[49, 50], and both products have been experimentally observed to coexist within the SEI[48]. Therefore, we consider Li_2BDC as the representative organic product in our model. The impact of Li-ion on EC reduction is considered, but the anions are not, as recent molecular dynamics simulations showed that the typical PF_6^- anions do not enter the electric double layer (EDL) in strong carbonate-based solvents[51]. The simplification treatment involves two procedures: (1) For two or more parallel reactions, we select the smallest reaction barrier as the simplified reaction barrier and record the Gibbs free energy change (parallel reactions have the same Gibbs free energy change); (2) For series reactions, we select the largest reaction barrier as the simplified reaction barrier and record the sum of Gibbs free energies for these series reactions.

In the phase-field simulations, we focus on the formation kinetics of organic Li_2BDC and inorganic Li_2CO_3 via the simplified reactions (R1, R2, and R3 in Fig. 2C) under a constant voltage of -3.04 V with respect to standard hydrogen electrode potential, SHE (or 0 V versus Li^+/Li^0). As illustrated in Fig. 1, we employ a 1-D system representing a half-cell, and the simulation domain spans from the Li metal electrode surface at $x = 0$ nm into the bulk liquid electrolyte comprised of EC and 1 M $LiPF_6$ at $x = 100$ nm. A set of non-conserved order parameters (ϕ_E,ϕ_{S1},ϕ_{S2}) represent the electrolyte (E), inorganic Li_2CO_3 (S1), and organic Li_2BDC (S2) phases, respectively. The phase evolution is governed by the Allen-Cahn equations (equations 3-5 in **Experimental**). The total Gibbs free energy change ΔG_m^r and the linearized reaction rate R_m for each reaction (m is the reaction index for R1, R2, and R3) are related to its standard Gibbs free energy change ΔG^0, reduction potential ψ^0, and the activation energy ΔG^* from DFT, as well as the local activities of species including electrons, Li^+ and EC molecules, as shown in equation 6 and equation 7 in **Experimental** section. Electron tunneling is a key short-term electron transport mechanism for

View Article Online
DOI: 10.1039/D5EE01030F

SEI formation, which is governed by the tunneling barrier of SEIs. Therefore, we numerically solve the steady-state Schrödinger electron tunneling equation by formulating a phase-dependent tunneling barrier to calculate the probability of electrons in the SEI, so that the SEI/electrolyte interface positions do not need to be explicitly tracked, taking advantage of phase-field modeling. The local electron activity can then be defined as the probability of electrons in SEI, i.e., $a_{e^-} = |\Psi^*\Psi|$, where Ψ is the electron wave function (see "Electrons tunneling" in **Experimental** for details). At the Li metal surface, the a_{e^-} is presumed to be 1 and decays exponentially through the SEI and electrolyte. The time-dependent evolution of the concentration distribution of Li^+ and EC is dominated by the reaction-diffusion equation (equation 9 in **Experimental** section), and the diffusivities of species are obtained from MD calculations (see "Species transport" in **Experimental** section for details). We assume the concentrations of Li^+ and EC at the Li/SEI interface are both 0 M. At the right electrolyte boundary, their concentrations are fixed at 1 M for Li^+ and 15 M for EC, corresponding to their initial bulk concentration. The activities of species are $a_i = x_i/x_i^0$, where x_i is the concentration of species Li^+ and EC, the standard concentration of Li^+ ($x_{Li^+}^0$) and EC (x_{EC}^0) are 1 M and 15 M, respectively. Therefore, the initial activities of both a_{Li^+} and a_{EC} are 1.

Electron tunneling effect on SEI thickness. SEI formation is initiated with the electrolyte reduction at the anode surface, where electrons are transferred from the anode via tunneling through the growing SEI layer. The electrolyte reduction products are precipitated on the anode surface, serving as a protective layer against further electrolyte decomposition, and the thickness of the SEI is determined by electron tunneling range. Therefore, in this section, we first investigate the effect of electron tunneling on the growth of both organic Li_2BDC and inorganic Li_2CO_3 via (R1) and (R3), respectively. We consider a 1-D system with different single SEI nucleus

View Article Online
DOI: 10.1039/D5EE01030F

representing the initial dense organic Li_2BDC and inorganic Li_2CO_3 seeds, as illustrated in Fig. 3A and 3B. To focus on investigating the electron tunneling behavior, we temporally disregarded the transport of Li^+ and EC during SEI growth by assuming that the activities of Li^+ and EC remains constant at its initial value ($a_{Li^+} = a_{EC} = 1$), mimicking a semi-infinite system with sufficient supplies of these species from the electrolyte. Thus, the Gibbs free energy changes of organic Li_2BDC (ΔG_{R1}^r) and inorganic Li_2CO_3 formation (ΔG_{R3}^r) from equation 6 in **Experimental** are modified as follows:

$$\Delta G_{R1}^r = \Delta G_{R1}^0 + F\left(\psi_e - \psi_{sol} - \psi_{R1}^0\right) - RT\ln a_{e^-} \tag{1}$$

$$\Delta G_{R3}^r = \Delta G_{R3}^0 + F\left(\psi_e - \psi_{sol} - \psi_{R3}^0\right) - 2RT\ln a_{e^-} \tag{2}$$

where F is the Faraday constant, R is the gas constant and T is the temperature.

To highlight the electron tunneling effect, we compare two cases: one assuming the electrons activity $a_{e^-} = 1$ throughout the system (i.e., assuming the SEI behaves like a metal), and the other with electron activity a_{e^-} obtained from the steady-state Schrödinger electron tunneling equation. As shown in Fig. 3C and 3D, starting with an initial thickness of 6 nm, the SEI will continuously grow when $a_{e^-} = 1$ until the electrolyte is fully consumed. However, when considering electron tunneling effect, both organic and inorganic SEI exhibit self-limiting growth behavior. They stop the initial quick growth after reaching a specific thickness. This occurs because, while the Gibbs free energy changes of reactions R1 and R3 (from equations 1 and 2) remain consistently negative, allowing the reactions to proceed indefinitely; but with electron tunneling, the electron activity decays exponentially as the SEI grows (Fig. S1). Once the electron activity reduces to a certain level (i.e., when $\Delta G_{R1}^r = 0$ and $\Delta G_{R3}^r = 0$ in equations 1 and 2), reactions R1 and R3 reach equilibrium, where the SEI reaches a tunneling-limited thickness and

View Article Online
DOI: 10.1039/D5EE01030F

stops further growth. In our model, the tunneling barriers for Li_2CO_3 ($\Delta E_{Li_2CO_3} = 1.78$ eV) is derived from DFT calculation[52]. The tunneling barrier for Li_2BDC is estimated to be a lower bound of $\Delta E_{Li_2BDC} = 0.24$ eV due to porosity[53] and the fact of the organic Li_2DEC, structurally close to Li_2BDC, has been experimentally measured to exhibit a tunneling barrier ~1 eV lower than of inorganic SEI components[54]. It aligns with the general trend that the inorganic component in SEI blocks electron tunneling more effectively than the organic species. Using these values, our model predicts tunneling-limited SEI thicknesses of ~29.4 nm and ~11 nm for Li_2BDC and Li_2CO_3, respectively, which are close to the experimentally reported values[29, 30] during SEI formation. These can be referred to as the "tunneling-limited thickness", which leads to a good estimation of the first cycle capacity loss, corresponding to the Li-consumed to form the SEI up to the tunneling-limited thickness, agreeing well with experiments[52, 55].

Fig. 3 also shows the time scale to grow the Li_2BDC and Li_2CO_3 layers to reach stable thickness. They are 66 ps and 20 ms for Li_2BDC and Li_2CO_3 layers, respectively, under the assumption of no concentration variation of Li^+ and EC during SEI growth. The electron tunneling generally occurs within a few attoseconds[56]. Consequently, this discrepancy in timescales is primarily attributed to the kinetic barrier of the single-electron reduction reaction (R1), substantially lower than that of the two-electron reduction reaction (R3), despite the overall Gibbs free energy of R3 being much greater than that of R1.

View Article Online
DOI: 10.1039/D5EE01030F

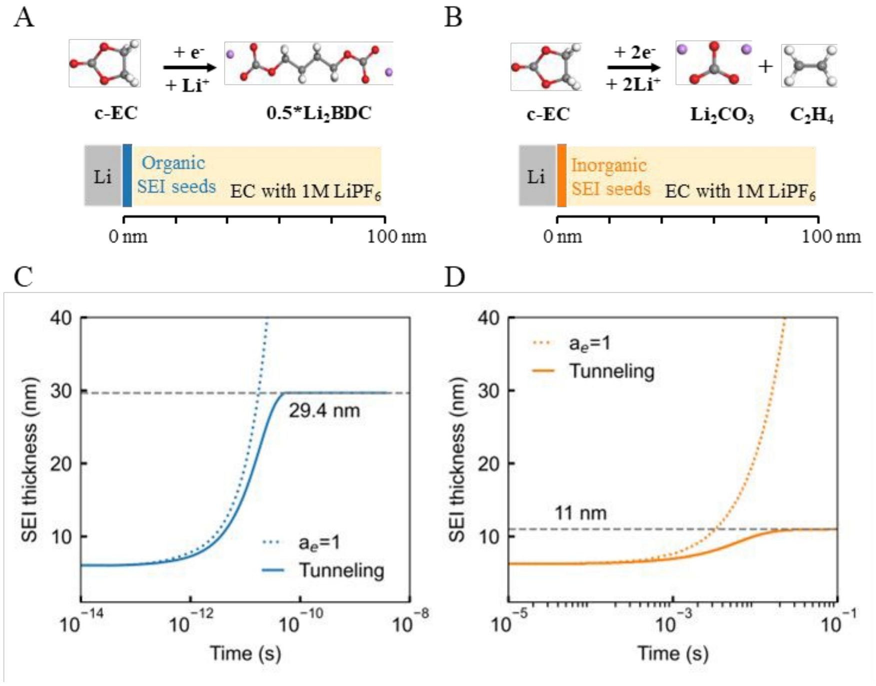

Fig. 3. The effect of electron tunneling on the growth of the organic Li_2BDC based on R1 and inorganic Li_2CO_3 based on R3. (A) and (B) illustrations of reactions R1 and R3 considered and the 1D system, respectively, (C) Comparison of organic Li_2BDC growth behaviors between assuming a_e- and electron tunneling, (D) Comparison of inorganic Li2$_{\text{CO}}$3 $_{\text{growth behaviors}}$ assuming and electron tunneling.a_e-

Effect of Li^+ and EC molecules on SEI formation rates. In addition to the electronic tunneling effect on SEI thickness, the evolution of the concentration of Li^+ and EC in the system is also critical to the growth dynamic of SEI products. To further investigate the governing factors for both organic and inorganic SEI growth kinetics, we performed a series of simulations by turning on/off the diffusivities of Li^+ and EC. By assuming the activity of species, we can compare four different cases: (1) Not e*volving both Li^+ and EC* ($a_{Li^+} = 1$ and $a_{EC} = 1$) means that the concentrations of Li^+ and EC remain constant as their initial values during SEI growth. Under this idealized condition, the reaction rate is governed mainly by charge-transfer kinetics. (2) *Only evolving EC* ($a_{Li^+} = 1$, and $a_{EC} \neq 1$ calculated by equation 9) represents the scenario where only the consumption of EC is considered while the Li^+ concentration remains at its initial value. The

View Article Online
DOI: 10.1039/D5EE01030F

reaction rate is affected by both charge-transfer kinetics and the local activity of EC. (3) *Only evolving Li*$^+$ ($a_{Li^+} \neq 1$ calculated by equation 9, and $a_{EC} = 1$) represents the scenario where only the consumption of Li$^+$ is considered while the EC concentration remains at its initial value. The rate is thus governed by charge-transfer kinetics and the local activity of Li$^+$. (4) *Evolving both Li*$^+$ *and EC* ($a_{Li^+} \neq 1$ and $a_{EC} \neq 1$ calculated by equation 9) indicates that both Li$^+$ and EC are consumed according to their stoichiometric ratio during SEI growth, and their concentration distributions over time are determined by the diffusion equation. Reaction rates in this case reflect a coupled control by charge-transfer kinetics and the activities all species. The simulation system is the same as those presented in Fig. 3A and 3B.

In case (1) shown in Fig. 4A, the organic SEI layer growth via R1 will reach their tunneling-limited thickness within around 66 ps (solid blue line), and its rate is purely governed by the reaction kinetics. Furthermore, we find that the EC diffusion has no significant effect on the Li$_2$BDC growth (the solid and dotted blue lines overlap) by comparing cases (1) and (2), as the EC concentration in electrolyte closely matches that in Li$_2$BDC, suggesting EC molecules could be reduced on-site without requiring additional EC supplied by the electrolyte. Considering the Li$^+$ consumption and diffusion by comparing cases (3) and (4), it is found that the predicted Li$_2$BDC growth time in Fig. 4A increased from 36 ns to ~57 μs (solid and dotted purple lines). This is consistent with the time scale (~ 29 μs) for Li$^+$ to diffuse from the right boundary of the electrolyte region to the Li$_2$BDC surface. It is estimated by using $\frac{L^2}{D^E_{Li^+}}$, where the L = 100 nm is the diffusion length, and $D^E_{Li^+}$ = 3.5×10^{-10} m^2/s is the diffusivity of Li$^+$ in electrolyte obtained from MD simulations. The simulated Li$_2$BDC growth time (~57 μs) is close to the $\frac{L^2}{D^E_{Li^+}}$ estimation, indicating the Li$^+$ diffusion-controlled growth nature. That is because, in contrast to EC, the Li site density

View Article Online
DOI: 10.1039/D5EE01030F

inside Li_2BDC (~13.5 M) is significantly higher than the initial concentration of Li^+ in the electrolyte (1 M) and the reaction rate of R1 is much faster than the Li^+ diffusion, which means that a large amount of Li^+ needs to be consumed to grow SEI, necessitating Li^+ diffusion from the electrolyte to the SEI/electrolyte interface to sustain Li_2BDC growth, as shown in Fig. S2A.

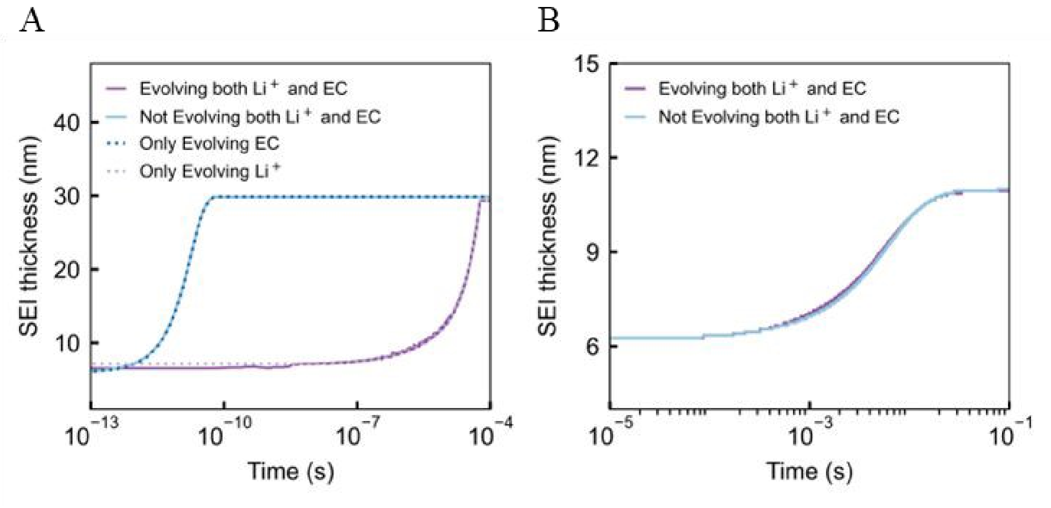

Fig. 4. 1-D phase-field simulation of the growth of the organic and inorganic SEI products, considering reactions R1 and R3 in Fig. 2C. Parameter study for the governing kinetic factors for organic Li_2BDC growth (A) and inorganic Li_2CO_3 growth (B). Four cases: (1) Not e*volving both Li*$^+$ *and EC* ($a_{Li^+} = 1$ and $a_{EC} = 1$): the concentrations of Li^+ and EC remain constant as their initial values during SEI growth; (2) *Only evolving EC* ($a_{Li^+} = 1$, and $a_{EC} \neq 1$ calculated by equation 9): only the consumption of EC is considered while the Li^+ concentration remains at its initial value; (3) *Only* e*volving Li*$^+$ ($a_{Li^+} \neq 1$ calculated by equation 9, and $a_{EC} = 1$): only the consumption of Li^+ is considered while the EC concentration remains at its initial value; (4) *Evolving both Li*$^+$ *and EC* ($a_{Li^+} \neq 1$ and $a_{EC} \neq 1$ calculated by equation 9): both Li^+ and EC are consumed according to their stoichiometric ratio during SEI growth.

Regarding the inorganic Li_2CO_3 growth via R3, the Li_2CO_3 layer grows to its tunneling-limited thickness of about 11 nm under ~ 20 ms, which is much slower than diffusion of both Li^+ (~ 29 μs) and EC, thus their diffusion does not influence the inorganic Li_2CO_3 SEI layer growth behavior (Fig. 4B and Fig. S2B). In contrast to the organic Li_2BDC, the growth rate of Li_2CO_3 is much (~10^3 times) slower due to the significantly larger kinetic barrier $\Delta G^*_{R3} = 0.72$ eV of R3 than

View Article Online
DOI: 10.1039/D5EE01030F

that of $\Delta G^{*}_{R3} = 0.15$ eV for R1. We further show that by increasing the Li^+ concentration from 1M to 4M, the time required for Li_2BDC to reach its stable thickness decreases from 57 μs to 1 μs, while the growth rate of dense Li_2CO_3 remains unchanged (Fig. S3). Consequently, the growth rate of Li_2BDC is determined by Li^+ diffusion, whereas the growth of Li_2CO_3 is controlled by the reaction rate.

Spatial, chemical, and temporal evolution of SEI. In the previous section, we separately investigate the effects of electron tunneling and species diffusion on the growth kinetics of single-layered dense organic Li_2BDC or inorganic Li_2CO_3 products. However, experimental studies indicate that the formed SEI often consists of a two-layer structure, with an inner inorganic layer and an outer organic layer that usually exhibits a porous structure[29, 30]. Therefore, it is crucial to study the spatial, chemical, and temporal evolution of the SEI layer, as well as the competition between products, to gain an in-depth understanding of the limiting processes, their interactions, and the final SEI composition and thickness. To this end, we analyze the temporal SEI formation via R1 to R3 based on Fig. 2C. Initially, we assume that there is a two-layer structured SEI nucleus within the simulation system, comprising a 0.5 nm dense Li_2CO_3 layer adjacent to the Li metal and a 6 nm thick layer of Li_2BDC at the outer layer with a constant porosity of 50%, as shown in Fig. S4. Subsequently, we calculate the SEI formation from nanoseconds to seconds. Fig. 5A illustrates the general trends of SEI thickness over time. Initially, from nanoseconds to microseconds, the porous Li_2BDC will grow to its stable thickness (~27.2 nm) via R1. After 21.7 μs, Li_2BDC near the Li metal side transforms into porous Li_2CO_3 via R2, growing to its stable thickness (~ 11 nm). After 1 ms, the pores in the porous Li_2CO_3 are filled via R3. The eventual SEI consists of a porous outer organic layer (~16.2 nm thick) and a thinner dense inner inorganic

View Article Online
DOI: 10.1039/D5EE01030F

layer (~11 nm) covering the anode surface. This aligns well with experimental finding of a two-layered structure[2, 5, 29].

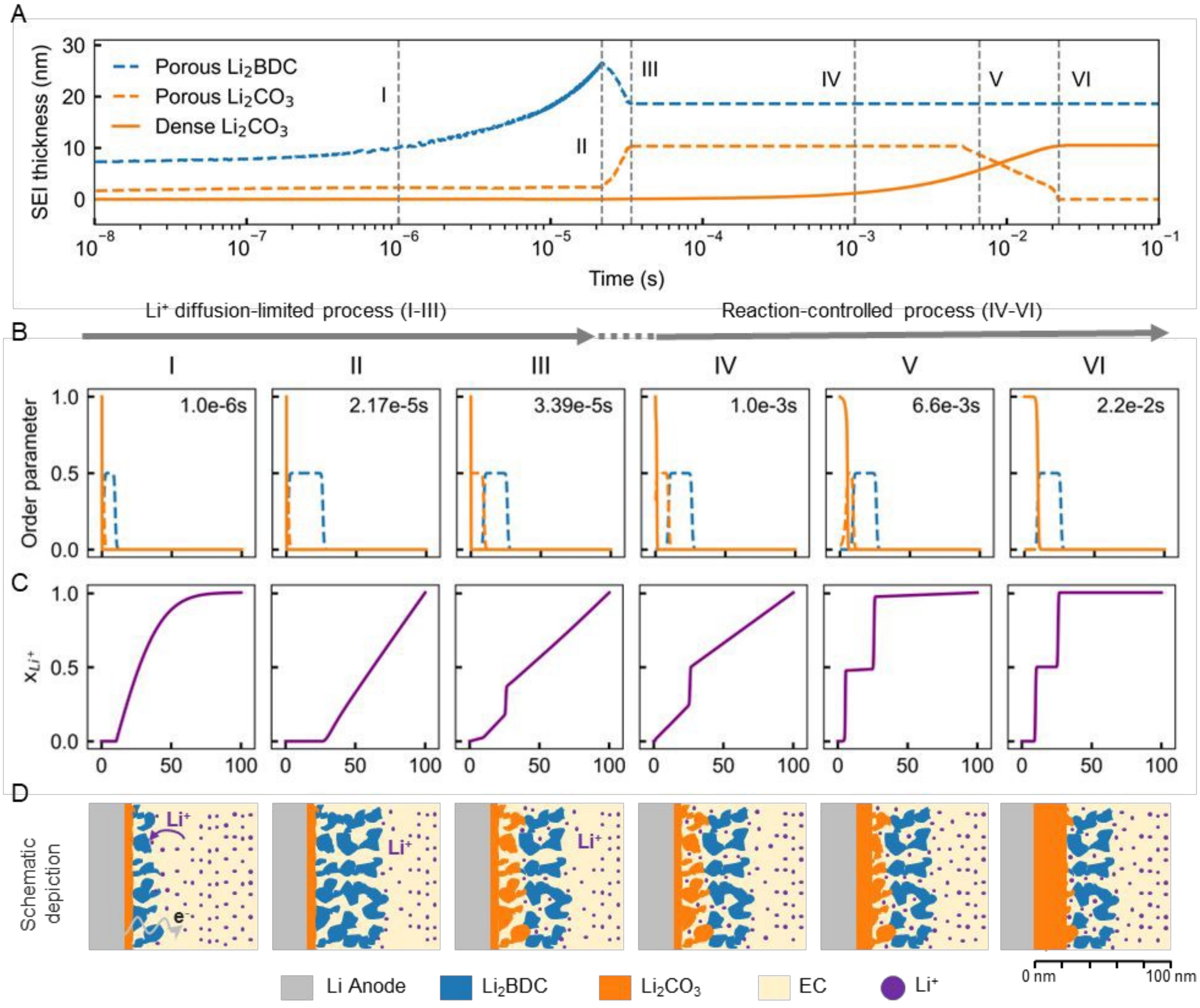

Fig. 5. Temporal evolution of SEI growth in Li/(EC + 1M $LiPF_6$) model system. (A) Temporal evolution of SEI thickness. The dashed and solid lines represent the porous and dense products, respectively. Temporal evolution of the order parameters (B) indicating the products and the concentration distribution of Li^+ (C) at 6 selected times. The position (0 ~ 100 nm) signifies the distance from the Li anode surface to the electrolyte region. (D) Schematic depiction of SEI growth in Li/(EC + 1M $LiPF_6$) model system from nanoseconds to seconds. Color scheme: gray for Li anode, blue for Li_2BDC, orange for Li_2CO_3, light yellow for EC, and purple for Li^+.

View Article Online
DOI: 10.1039/D5EE01030F

To understand the underlying processes governing SEI formation, we conduct a detailed analysis of the temporal evolution in the distribution of chemical reaction species and SEI products, as shown in Fig. 5B and 5C. The corresponding SEI morphologies at 6 selected time frames are displayed in Fig. 5D. The diffusion rate of Li^+ is slower than EC decomposition via R1 as the porous Li_2BDC products gradually grow. As a result, Li^+ ions are immediately consumed when they arrive at the SEI/electrolyte interface, leading to a concentration gradient in the electrolyte zone from 1 μs to 21.7 μs (stage I to II). This indicates that Li_2BDC production is a Li^+ diffusion-limited process. Despite the charge-transfer rate for the R2 pathway being slightly slower than that of R1, the formation of Li_2CO_3 via R2 does not occur in this stage due to limited Li^+ availability as Li^+ is preferentially consumed by the faster-growing R1 process. After 21.7 μs, when Li_2BDC reaches its tunneling-limited thickness, additional Li^+ begins to diffuse into this porous layer (stages II to III), enabling Li_2BDC to react with Li^+ and electrons to form Li_2CO_3 via R2, the overall process still remains diffusion-limited. After ~ 0.02s, Li_2CO_3 can be generated inside the pores. Since direct two-electron reduction of EC to Li_2CO_3 via R3 has a much slower charge-transfer rate, the Li^+ diffusion from the electrolyte rapidly compensates for the consumption of Li^+ during the two-electron reduction of EC, which is a reaction-controlled process (stage IV to VI), as shown in Fig. 5C. In contrast to the Li^+ concentration profiles, no EC-concentration gradient develops during the entire process, as shown in Fig. S5. From this, we conclude that the first two steps of one electron reduction process including the electrolyte degradation to organic Li_2BDC and transformation to $Li_2CO_{3,}$ are Li^+ diffusion-limited process (Stage I to III), after that, the two electrons reduction reaction that directly formed dense Li_2CO_3 is reaction-controlled process (Stage IV to VI).

View Article Online
DOI: 10.1039/D5EE01030F

Furthermore, after 0.02 s, the Li metal surface is fully covered with SEI products and the EC can no longer be reduced due to the block of electron tunneling. This indicates that the initial SEI formation is completed within this short time frame, which agrees with the experimental results [7, 57]. Direct in-situ measurements of the initial SEI formation are rather challenging, as these reactions occur very fast[58], as pointed out by Odziemkowski and Irish[7], who tracked the corrosion potential time transients of Li-metal electrode in various electrolyte systems and indicated that the passivating reactions, which lead to SEI formation, are often completed in less than 1 second. The two-layered SEI model, with the inorganic species (LiF, Li_2CO_3, Li_2O) close to the electrode surface and the porous organic layer (e.g. LEDC) closer to the electrolyte, obtained from postmortem analysis, does not reveal the formation sequence and timelines of these species[59]. Notably, the absence of operando tools with nanosecond-to-second temporal resolution and nanoscale chemical specificity is a well-recognized gap field[3]. Recently, the formation sequence obtained from gas evolution combined with other spectroscopy analysis revealed LEDC as the major product with little Li_2CO_3 during initial SEI formation, and LEDC eventually evolved into Li_2CO_3[60-63]. Using isotope exchange along with in situ time-of-flight secondary ion mass spectroscopy (TOF-SIM) measurements, a bottom-up SEI growth mechanism was proposed, suggesting the SEI components formed in the early stage (organic species) are on the outside (electrolyte side), while those formed in the latter stage (inorganic species) are on the inside (electrode side)[64]. These experimental results on the temporal and spatial evolution of SEI formation collectively support the prediction from our atomically informed phase-field model (AIPFM). This sequence, LEDC forms first and converts to Li_2CO_3 near the electrode surface, is different from the CRN-kMC, which predicted that LEDC continues to grow after Li_2CO_3 stops growing[31].

View Article Online
DOI: 10.1039/D5EE01030F

Influence of key parameters on the SEI growth dynamic. Having elucidated the growth dynamics and governing mechanisms of SEI formation on Li metal in EC with $LiPF_6$, we further employ our model to explore how key parameters, including electron tunneling barriers (ΔE), species diffusivities, and reaction kinetic barriers (ΔG^*), affect SEI evolution.

The relative tunneling barriers play an important role in determining SEI morphology. Higher electron-tunneling barriers led to a thinner Li_2BDC layer via R1 and Li_2CO_3 layer via R3 and shorter time to reach the tunneling-limited thickness (Fig. S6A-C). Since the tunneling barrier of the organic phase (Li_2BDC) is more susceptible to factors such as porosity and electrolyte composition[53], while only varying $\Delta \mathrm{E}_{\mathrm{Li_2BDC}}$ from 0.24 to 1.8 eV. The overall SEI formation sequence remained the same: rapid porous Li_2BDC deposition via R1, partial conversion to Li_2CO_3 via R2, and final pore filling by Li_2CO_3 via two-electron EC reduction in R3. However, the bilayer morphology was only formed when $\Delta E_{Li_2BDC} < \Delta E_{Li_2CO_3}$. Conversely, when $\Delta E_{Li_2BDC} \geq \Delta E_{Li_2CO_3}$, a thinner initial Li_2BDC layer is ultimately fully consumed and converted to a thicker dense Li_2CO_3 layer, yielding a predominantly single inorganic SEI layer (Fig. S8). These results underscore the critical role of relative tunneling barriers in determining SEI morphology.

The effect of Li^+ diffusivity on SEI growth has also been systematically examined. Increasing Li^+ diffusivity in the liquid electrolyte from 10^{-11} m^2/s to 10^{-8} m^2/s significantly accelerates Li_2BDC growth via R1, reducing the growth timescale from ~10^{-4} s to ~10^{-7} s (Fig. S9A), with no impact on the Li_2CO_3 growth via R3, as it is governed by the reaction kinetics rather than diffusion (Fig. S9C). Notably, variations in Li^+ diffusivity within both solid phases have negligible influence on both Li_2BDC and Li_2CO_3 growth (Fig. S9B and S9D), further underscoring that liquid-phase Li^+ transport is the rate-limiting step for initial organic SEI formation.

View Article Online
DOI: 10.1039/D5EE01030F

Additionally, Li^+ diffusivity has a minimal influence on the SEI growth sequence and resulting bilayer architecture (Fig. S10).

We further evaluated the impact of the charge-transfer kinetic barrier (ΔG^*) on SEI growth by sweeping ΔG^* from 0.15 to 0.75 eV for both Li_2BDC (R1) and Li_2CO_3 (R3). This range corresponds to a decrease in the intrinsic electron-transfer rate constant k_m^0 from 2.08×10^{10} 1/s to 1.736 1/s. As shown in Fig.S11, two kinetic regimes emerge: (i) Li^+-diffusion-limited region: for lower ΔG^*, both SEI products reach their tunneling-limited thickness around the same time and remain largely insensitive to ΔG^*. (ii) Charge-transfer kinetic-limited: for higher ΔG^*, the growth rates of both Li_2BDC and Li_2CO_3 decrease exponentially with increasing ΔG^*. The transition occurs at $\Delta G^* \approx 0.49$ eV, where the calculated charge-transfer reaction rate equals the Li^+ diffusion rate, delineating the shift between Li^+-diffusion and electron-transfer-controlled regimes (Fig. S11C). These results highlight variations in kinetic barriers for each reaction, and their relative relationship to Li^+ diffusion rates, can lead to multiple rate hierarchies among R1-R3, ultimately altering the overall SEI growth sequence and one-layer or two-layer SEI structures.

It should be clarified that our simulations focus on the initial formation of the SEI, occurring on the timescale of seconds. Although our phase-field model can simulate and demonstrate the SEI evolution from nanoseconds to seconds, this self-limiting behavior is featured only during the initial short-term growth of SEIs. Ideally, the SEI would stabilize after intimal formation, preventing further Li^+ consumption and electrolyte degradation, since it is electronic insulating. However, SEI layer thickness can change during cycling and calendar aging[3]. Slower electron leakage mechanisms through hole polarons migration[65], the formation and transport of Li-atom interstitials[66], radical species shuttling[53], as well as grain boundaries[67, 68]. Qi *et al.*[69] reported that Li atoms can diffuse through the SEI via interstitial mechanisms, forming positive-

View Article Online
DOI: 10.1039/D5EE01030F

charged Li interstitials and electrons. A continuum model[20] predicted that the SEI can continue to grow to 1400 nm in 1000 days, where the neutral Li atoms carrying electrons facilitate this long-term SEI growth. Moreover, defects such as grain boundaries and heterogeneous interfaces[67], cracks, and pores[70] can serve as short-circuit transport paths for electrons and other reacting species. These mechanisms lead to continuous "growth" of the SEI as the battery degrades. We intend to thoroughly investigate these possibilities in our forthcoming study with a 2-D model.

The major strength demonstrated by this model framework is its ability to resolve the spatial and temporal evolution of SEI composition and thickness that span from nanoseconds to seconds, and deconvolute the interplay among multiple physics (reactions, species transport, electron tunneling), as well as reveal the governing factors for each electrolyte degradation process. Although this deconvolution provides insights into the governing mechanisms of electrolyte decomposition that are currently inaccessible to experimental microscopy or spectroscopy techniques, the predictions from our simulations, such as the initial SEI formation and thickness of SEI within milliseconds and the preferential formation of inorganic vs. organic products near the Li surface, serve as testable hypotheses for future experimental studies and can guide experimentalists by identifying key mechanistic signatures to be probed indirectly through ex situ quenching or rapid-interruption experiments followed by surface analysis.

The modeling framework developed in this study is broadly extensible to other electrochemical systems beyond lithium-based batteries, owing to two central features. First, it is explicitly informed by DFT calculations, which capture the chemical changes at the electrode/electrolyte interface. Second, the model is formulated as a general multiphase, multicomponent phase-field framework capable of capturing complex couplings among interfacial reactions, species transport, and microstructural evolution. To adapt this framework to other

View Article Online
DOI: 10.1039/D5EE01030F

electrochemical systems, such as sodium-ion, lithium-sulfur, or solid-state batteries, the key steps involve determining the reaction networks and corresponding parameters via DFT calculations, redefining the phase-field variables to reflect the relevant phases, and modifying the free energy functional to include new phases and reaction intermediates. Transport parameters (e.g., diffusivities, electron tunneling barrier) can be similarly updated to reflect system-specific physical properties. For instance, the same model structure can simulate Na SEI formation by introducing Na-containing decomposition reactions and products (e.g., Na_2CO_3, Na_2O[71]) and recalibrating the thermodynamic driving force and reduction kinetics accordingly. In solid-state systems, the framework can be further extended to include coupled electrochemical-mechanical effects by incorporating additional mechanical energy terms or coupling coefficients in the free energy functional, thereby enabling the simulation of multiple phases evolution at the solid-solid interface. By extending to higher dimensional simulations, it can potentially capture the detailed SEI morphology and its competition with Li stripping/plating. Combining this model with high-throughput calculations and virtual screening for materials discovery would provide data-based design guidance.

Conclusions

In summary, we present an atomically informed phase-field framework that reveals SEI evolution across unprecedented time scales (from nanoseconds to seconds) and length (from angstroms to 100 nm) and. Initially, porous Li_2BDC grows to ~27.2 nm via one-electron reduction within microseconds. After 21.7 μs, part of the Li_2BDC near the Li metal converts into porous Li_2CO_3 (~11 nm). By 1 ms, the pores are filled with Li_2CO_3 directly via two-electron reduction, forming a final SEI with a porous organic outer layer (~16.2 nm) and a dense inorganic inner layer (~11 nm). Li_2BDC formation and its transformation into Li_2CO_3 are limited by Li^+ diffusion, while

View Article Online
DOI: 10.1039/D5EE01030F

the final two-electron reduction of EC to form Li_2CO_3 is reaction-controlled. Electron tunneling determines the thickness of both layers. This study enhances understanding of SEI formation and demonstrates potential for simulating complex reaction networks across broad time and length scales.

View Article Online
DOI: 10.1039/D5EE01030F

Experimental

Phase-field model.

We formulate the phase-field model by considering the simplified reaction networks as well as the reacting species Li^+, e^- and EC, based on our recently developed phase-field model of stoichiometric compounds and solution phases[72]. With this approach, the phase-field governing equations can be directly derived via the variational derivatives of the free energies without any approximation or arbitrary treatments. The thermodynamic and kinetic parameters of the simplified reactions are shown in Fig. 2C and Table S2. We also consider the following assumptions/simplifications:

- The SEI products are considered stoichiometric compounds whose free energy only exists at their stoichiometric composition points rather than being a continuous function of composition, as shown in Fig. S6. Meanwhile, the electrolyte is assumed to be an ideal solution, whose realistic interaction behavior will be investigated in our future work using MD simulations or Debye-Hückel approximations. The Li metal anode is assumed to be at the left boundary of the simulation region and not explicitly simulated.
- The electric potential is assumed uniform within the electrolyte and SEI. Therefore, the applied voltage is imposed, and the Poisson equation is not solved, which significantly improves numerical efficiency and stability. The electron transport within the system is assumed to be dominated by tunneling.
- To improve numerical convergence, we use linear kinetics for most of the simulations involving SEI products in this work.
- The organic Li_2BDC is inherently micro-porous due to molecular disorder and low packing density. In our 1D model, porosity represented by fixed value rather than explicitly evolving

View Article Online
DOI: 10.1039/D5EE01030F

pore structures, which is a common simplification in 1-D SEI simulations[18, 22]. Thus, the porous SEI layer is considered as a mixture of electrolyte and solid products. While the current framework does not incorporate dynamic porosity, it retains the ability to resolve the competitive formation, spatial distribution, and temporal evolution of major inorganic and organic SEI species.

- The evolution of gas-phase (e.g. C_2H_4) is neglected because they escape from the SEI or system and do not contribute to further reactions and SEI film[31]. Their formation energies and reaction barriers are still accounted for when selecting the dominant solid-phase pathways, influencing the free energy landscape and kinetics of the phase-field model. Thus, neglecting explicit gas-phase evolution has minimal impact on the predicted solid-state SEI growth kinetics.
- The decomposition of both lithium hexafluorophosphate ($LiPF_6$) and the formed SEI products (i.e., Li_2O) is not considered in this model. We assume that the diffusion and dissolution of primary electrolyte reduction products (Li_2CO_3 and Li_2BDC) products formed during SEI formation are ignored due to relatively low solubility[73, 74].

Three phases are distinguished by a set of non-conserved order parameters, in which $(\phi_E,\phi_{S1},\phi_{S2}) = (1,0,0),(0,1,0),(0,0,1)$ represent the liquid electrolyte (E), Li_2CO_3 (S1) and Li_2BDC (S2) phases, respectively. The kinetic evolution of the primary order parameters ξ is governed by the following Allen-Cahn equations[72],

$$\frac{\partial \phi_E}{\partial t} = - L_E\left(\frac{\partial g_{well}}{\partial \phi_E} - \kappa_E \nabla^2 \phi_E\right) \tag{3}$$

$$\frac{\partial \phi_{S1}}{\partial t} = - L_{S1}\left(\frac{\partial g_{well}}{\partial \phi_{S1}} - \kappa_{S1} \nabla^2 \phi_{S1}\right) + h'(\phi_{S1})(R_2 + R_3) \tag{4}$$

View Article Online
DOI: 10.1039/D5EE01030F

$$\frac{\partial \phi_{S2}}{\partial t} = -L_{S2}\left(\frac{\partial g_{well}}{\partial \phi_{S2}} - \kappa_{S2}\nabla^2\phi_{S2}\right) + h'(\phi_{S2})(R_1 - R_2) \qquad (5)$$

where g_{well} is a multi-well function to ensure the local minima are at the above-mentioned order parameter values, κ_i represents the gradient coefficients which are related to the interfacial energies and thicknesses, $h(\phi) = 6\phi^5 - 15\phi^4 + 10\phi^3$ is an interpolation function, L_j is the interface mobility coefficient. The detailed derivation can be found in Supplementary note 1.

The total Gibbs free energy change ΔG_m^r and the linearized reaction rate R_m of reactions R1 to R3 can be written as,

$$\Delta G_m^r = \Delta G_m^0 + F\left(\psi_e - \psi_{sol} - \psi_m^0\right) - RT\ln\left(\prod_k^{reactants} a_k^{v_k^m} \prod_l^{products} a_l^{v_l^m}\right) \qquad (6)$$

$$R_m = -k_m^0 \frac{\Delta G_m^r \Delta G_m^r}{RT \quad RT} \qquad (7)$$

Where $k_m^0 = \frac{k_B T}{h} exp\left(-\frac{\Delta G_m^*}{RT}\right)$ is the electron transfer kinetic with the unit of (1/s), ΔG_m^* is the kinetic barrier of the electron transfer, *m* is the reaction index from R1 to R3, *F* is Faraday constant, ψ_e is the electric potential in the electrode, ψ_{sol} is the electric potential in the electrolyte, ψ_m^0 is the reduction potential vs. SHE; ΔG_m^0 is the standard Gibbs free energy change, *R* is the ideal gas constant, *T* = 298 K is temperature, a_k and a_l are the activities of the reactants and products of a given reaction, and v_k^m is the stoichiometric coefficient for species *k* in reaction *m*, which is positive for the reactants and negative for the products. In this work, we simulate the SEI formation under a constant voltage at -3.04 vs. SHE (i.e., 0 V versus Li^+/Li^0). Under this voltage, the overpotential of reaction $Li^+ + e^- = Li$ is 0, which means the $\psi_e - \psi_{sol} - \psi_{Li^+/Li^0}$ (vs. SHE) = 0 V. The interfacial potential difference at Li metal and electrolyte interface is thus $\psi_e - \psi_{sol} = -3.04$ V.

View Article Online
DOI: 10.1039/D5EE01030F

Electron transport. To describe the electron tunneling from Li metal through the SEIs and electrolyte behavior, we develop a diffuse-interface description of the steady-state Schrödinger equation with a phase-dependent tunneling barrier,

$$\nabla^2\Psi - \frac{2m_e}{\hbar^2} \cdot \Delta E_t(\{\phi_i\}) \cdot \Psi = 0 \tag{8}$$

where Ψ is the electron wave function, m_e is the electron mass, $\hbar$ is the reduced Planck constant, and $\Delta E_t(\{\phi_j\}) = \sum_j \Delta E_{tj}^0 h(\phi_j)$ is the phase-dependent tunneling barrier with ΔE_{tj}^0 being the electron tunneling barrier for each phase. The electron tunneling barrier for porous structure is assumed to be a constant, without explicitly accounting for the local variations introduced by solvent-filled pores[53, 75]. As the 1D model does not resolve the pore geometry, the uniform electron tunneling barrier is a reasonable assumption[76]. As such, the Schrödinger electron tunneling equation is numerically solved for the entire system without the need to distinguish the different phase regions and phase interfaces. The local electron activity can then be defined as the probability of electrons in SEI, i.e., $a_{e^-} = |\Psi^*\Psi|$. This numerical solution to the Schrödinger equation indicates an exponential decay of electron concentration at the SEI/electrolyte interface with the increase of SEI thickness, which would lead to extremely low electron concentrations when the SEI becomes thicker than its tunneling-limited thickness d_{lim}, and cause the SEI to shrink. However, the electron concentration is lower bounded by the intrinsic electron concentration of the SEI and electrolyte. Therefore, in the phase-field simulations, we use $a_{e^-} = |\Psi^*\Psi|$ with a lower cut-off of $a_{e^-}^{lim}$ that ensures $\Delta G_m^r = 0$ and an equilibrium SEI thickness of d_{lim} to avoid the SEI shrinkage.

Species transport. The time-dependent evolution of the concentration distribution of Li$^+$ and EC is dominated by diffusion. We directly evolve the reduced concentration $x_i = c_i/c_0$ in the

View Article Online
DOI: 10.1039/D5EE01030F

electrolyte rather than the total concentration, which follows the following reaction-diffusion equation.

$$h(\phi_E)\frac{\partial x_i}{\partial t} = \nabla \cdot \left(D_i^{eff} \nabla x_i\right) - x_i \frac{\partial h(\phi_E)}{\partial t} - \sum_j^{M,S1,S2} \frac{c_i^j}{c_0} \frac{\partial h(\phi_j)}{\partial t} \tag{9}$$

where $i = [Li^+, EC]$ is the concentration of species, and $c_0 = 1$M is the bulk concentration of Li$^+$, c_i^j is the site density in phase j. D_i^{eff} is the effective diffusion coefficient of species i, which is given by, $D_i^{eff} = h(\phi_{S1})D_i^{S1} + h(\phi_{S2})D_i^{S2} + h(\phi_E)D_i^E$. The diffusion coefficient of species (Li$^+$ and EC) in porous structure is calculated by $D_i^{S2} = P^{1.5}D_i^E$ based on the Bruggeman relation[77]. However, it is difficult to obtain a specific porosity of the outer organic layer, since the morphology and the porosity vary during the SEI formation [29, 30, 78, 79]. In this work, we assume the porosity (*P*) of the formed porous organic SEI layer is a constant of 50%. The self-diffusion coefficients of independent species can be found in Table S3 in *Supplementary Materials.*

Atomistic simulations

Density functional theory (DFT) calculations for ΔG^0 and ψ^0. All DFT calculations were conducted using Gaussian 09 code[80]. The double hybrid functional M06-2X[81-84], the basis set 6-31+G(d,p) together with the D3 dispersion correction[85] were used. The SMD solvation model[86] was used to account for the solvation environment with the dielectric constant set to ε=20.5 for the carbonate-based electrolyte[87, 88]. The standard Gibbs free energy change (ΔG^0) of the Li$^+$ coordination reaction (the only chemical reaction considered in this work) is calculated as the Gibbs free energy difference between the product and the reactants. The Li$^+$ coordination reaction was considered barrierless[31]. The reduction potential of an electrochemical reaction with respect to the standard hydrogen electrode (SHE) was calculated via $\psi^0 = -\Delta G^0/F - 4.44$. The calculation results of all the reactions in Figure 2A are listed in Table S1.

View Article Online
DOI: 10.1039/D5EE01030F

Kinetic barrier ΔG^* for electron transfer. The Marcus theory[44, 45] was used to calculate the kinetics of reduction reactions. Specifically, it is assumed that all reduction reactions occur heterogeneously, with electrons transferred from the electrode[89]. The energy barrier ΔG^* for a reduction reaction is,

$$\Delta G^* = \frac{\lambda}{4}\left[1 + \frac{\Delta G^0}{\lambda}\right]^2 \tag{10}$$

where λ is the reorganization energy, which can be decomposed into the inner-shell reorganization energy λ_{in} and a bulk outer-shell reorganization energy λ_{out} ($\lambda = \lambda_{in} + \lambda_{out}$). The four-point method of Nelsen[90] is used to approximate the inner-shell electron reorganization energy, while Marcus's expression is used for the outer-shell term[31, 89]:

$$\lambda_{out} = \frac{(\Delta e)^2}{8\pi\varepsilon_0}\left(\frac{1}{r} - \frac{1}{2D}\right)\left(\frac{1}{\varepsilon} - \frac{1}{\varepsilon_s}\right) \tag{11}$$

where Δe is the transferred electron (that is e for each one-electron reduction reaction), ε_0 is the vacuum permittivity (8.85×10^{-12} F/m), r is the radius of the reacting molecule and its first solvation shell (all assumed to be 5.0 Å for simplicity[31]), D is the molecule-electrode distance (set to 5.0 Å for calculating λ_{out}), ε is the optical dielectric constant (~2.0)[31] and ε_s is the static dielectric constant (taken to be 20.5)[87, 88]. The calculation results of all the reactions are shown in Fig. 2A.

Molecular dynamics simulations of diffusion coefficients. MD simulations were conducted to calculate the diffusion coefficients of Li^+ and EC in the bulk electrolyte following our recent work[51]. To be more specific, MD simulations were carried out through the Forcite module as implemented in the Materials Studio (MS) 2020[54] with COMPASS III force field[91] and a charge scale of 0.7 applied to the salt ions[51]. The atomistic model for the carbonate-based

View Article Online
DOI: 10.1039/D5EE01030F

electrolyte was constructed to be ~1.0 M $LiPF_6$ salt dissolved in the mixed solvent composed of 30 vol % EC and 70 vol % EMC. The MD simulations were first conducted under the constant particle number, volume, and temperature (NPT) ensemble for 2.0 ns at room temperature (20 ℃). Then production runs under the NPT ensemble were conducted for 4.0 ns for statistical analyses to obtain the diffusion coefficients of Li^+, and EC following the approach proposed in a recent work[92]. The calculation results are listed in Table S2.

Model Implementation

The simulations are performed using COMSOL Multiphysics based on the finite element method. A one-dimensional model with a size of 100 nm is built in this work and the simulation domain is discretized by grid spacing of 0.5 nm. Zero-flux boundary conditions are applied for order parameters (ϕ_E,ϕ_{S1},ϕ_{S2}) at the left and right boundaries. The Li^+ concentration in the electrolyte drops during SEI formation due to the consumption of large amounts of Li^+ ions, a new equilibrium needs to be established by stripping some Li^+ into the electrolyte. The equilibrium Li-plating/stripping potential will shift due to the Li^+ activity. However, the stripping of Li^+ during initial SEI formation under potentiostatic voltages can be safely ignored, as the reaction rate of lithium deposition and stripping is much lower than that of SEI formation[35]. Hence, we assume the Li^+ and EC concentrations at the Li metal surface are both 0 M. The concentrations of Li^+ and EC at the right electrolyte boundary are 1 M and 15 M, respectively, corresponding to their initial bulk concentration. The activity coefficients of Li^+ and EC are 1 and 15, respectively. The boundary condition for solving the steady-state Schrödinger equation is defined to maintain $\Psi = 1$ (to mimic pure Li metal) at the left boundary of our 1-D simulation region, and $\frac{\partial \Psi}{\partial x} = 0$ at the right

View Article Online
DOI: 10.1039/D5EE01030F

boundary. These boundary conditions are shown in Fig. 1. The phase-field parameters are summarized in Table S3 in *Supplementary Materials*.

Lead contact

Further information and request for resources should be directed to and will be fulfilled by the lead contact, Yue Qi (yueqi@brown.edu) and Long-Qing Chen (lqc3@psu.edu)

Author contributions

K.N.Z.: Methodology, Investigation, Data Curation, Writing – Original Draft, Visualization; Y.Z.J.: Conceptualization, Methodology, Investigation, Writing – Review & Editing, Supervision; Q.S.W.: Methodology, Investigation, Data Curation, Writing – Review & Editing; S.A.N.: Methodology; L.Q.C. and Y.Q.: Conceptualization, Methodology, Resources, Writing – Review & Editing, Supervision, Project Administration, Funding Acquisition

Declaration of interests

While the work was performed when Dr. Janzhou Ji was at Penn State. His current affiliation is Ohio State University, Columbus, OH, USA. While the work was performed when Dr. Seyed Amin Nabavizadeh was at Penn State. His current affiliation is GE Power, Greenville, SC, USA. While the work was performed when Dr. Qisheng Wu was at Brown. His current affiliation is Suzhou Laboratory, Jiangsu, China.

View Article Online
DOI: 10.1039/D5EE01030F

Data and Code availability

The first-principles computational results on the structure of reaction products and the COMSOL input file for this model are available in the NOMAD repository at https://nomad-lab.eu/prod/v1/gui/user/uploads/upload/id/I6rPnwjtTAOafwYpwN_qPQ

Acknowledgment

We also thank Dr. John Lawson, Dr. Mehta, and Dr. Joakim H. Stenlid from NASA, as well as Dr. Kang Xu from the SES AI Corp for stimulating discussions and reviewing the manuscript.

The authors acknowledge financial support from NASA under grant number 80NSSC21M0107. K.N.Z. and L.Q.C. also appreciate the generous support from the Donald W. Hamer Foundation through a Hamer Professorship at Penn State. The computations were performed on the Roar supercomputers at Penn State and the Center for Computation and Visualization (CCV) at Brown.

References

1. X. B. Cheng, R. Zhang, C. Z. Zhao, F. Wei, J. G. Zhang and Q. Zhang, *Advanced Science*, 2016, **3**, 1-20.
2. P. Verma, P. Maire and P. Novák, *Electrochimica Acta*, 2010, **55**, 6332-6341.
3. A. Wang, S. Kadam, H. Li, S. Shi and Y. Qi, *npj Computational Materials*, 2018, **4**, 15-15.
4. H. Wu, H. Jia, C. Wang, J. G. Zhang and W. Xu, *Advanced Energy Materials*, 2021, **11**, 1-35.
5. K. Xu, *Chemical Reviews*, 2014, **114**, 11503-11618.
6. X. Cui, S. D. Kang, S. Wang, J. A. Rose, H. Lian, A. Geslin, S. B. Torrisi, M. Z. Bazant, S. Sun and W. C. Chueh, *Joule*, 2024, DOI: 10.1016/j.joule.2024.07.024.
7. M. Odziemkowski and D. E. Irish, *Journal of The Electrochemical Society*, 1992, **139**, 3063.
8. A. Yulaev, V. Oleshko, P. Haney, J. Liu, Y. Qi, A. A. Talin, M. S. Leite and A. Kolmakov, *Nano Letters*, 2018, **18**, 1644-1650.
9. D. T. Boyle, Y. Li, A. Pei, R. A. Vila, Z. Zhang, P. Sayavong, M. S. Kim, W. Huang, H. Wang, Y. Liu, R. Xu, R. Sinclair, J. Qin, Z. Bao and Y. Cui, *Nano Letters*, 2022, **22**, 8224-8232.
10. T. Li and P. B. Balbuena, *Chemical Physics Letters*, 2000, **317**, 421-429.
11. Y. Wang, S. Nakamura, M. Ue and P. B. Balbuena, *Journal of the American Chemical Society*, 2001, **123**, 11708-11718.
12. J. Halldin Stenlid, P. Žguns, D. Vivona, A. Aggarwal, K. Gordiz, Y. Zhang, S. Pathak, M. Z. Bazant, Y. Shao-Horn, A. Baskin and J. W. Lawson, *ACS Energy Letters*, 2024, **9**, 3608-3617.
13. O. Borodin and G. D. Smith, *J. Phys. Chem. B.*, 2009, **113**, 1763-1776.
14. K. Tasaki, *Journal of Physical Chemistry B*, 2005, **109**, 2920-2933.
15. J. W. Abbott and F. Hanke, *J. Chem. Theory Comput.*, 2022, **18**, 925-934.
16. Y. Liu, P. Yu, Y. Wu, H. Yang, M. Xie, L. Huai, W. A. Goddard, 3rd and T. Cheng, *J. Phys. Chem. Lett.*, 2021, **12**, 1300-1306.
17. F. Ospina-Acevedo, N. Guo and P. B. Balbuena, *Journal of Materials Chemistry A*, 2020, **8**, 17036-17055.
18. P. J. Weddle, E. W. C. Spotte-Smith, A. Verma, H. D. Patel, K. Fink, B. J. Tremolet de Villers, M. C. Schulze, S. M. Blau, K. A. Smith, K. A. Persson and A. M. Colclasure, *Electrochimica Acta*, 2023, **468**.
19. D. Li, D. Danilov, Z. Zhang, H. Chen, Y. Yang and P. H. L. Notten, *J. Electrochem. Soc.*, 2015, **162**, A858-A869.
20. J. Christensen and J. Newman, *Journal of The Electrochemical Society*, 2004, **15**, A1977-A1988.
21. B. Horstmann, F. Single and A. Latz, *Current Opinion in Electrochemistry*, 2019, **13**, 61-69.
22. F. Single, B. Horstmann and A. Latz, *Journal of The Electrochemical Society*, 2017, **164**, E3132-E3145.
23. L. von Kolzenberg, A. Latz and B. Horstmann, *ChemSusChem - Chemistry Europe*, 2020, **13**, 3901-3910.
24. M. Uppaluri, K. Shah, V. Viswanathan and V. R. Subramanian, *Journal of The Electrochemical Society*, 2022, **169**.
25. M. Safari, M. Morcrette, A. Teyssot and C. Delacourt, *Journal of The Electrochemical Society*, 2009, **156**.
26. R. Li, S. O'Kane, M. Marinescu and G. J. Offer, *Journal of The Electrochemical Society*, 2022, **169**.
27. M. Gerasimov, F. A. Soto, J. Wagner, F. Baakes, N. Guo, F. Ospina-Acevedo, F. Röder, P. B. Balbuena and U. Krewer, *The Journal of Physical Chemistry C*, 2023, **127**, 4872-4886.
28. J. Wagner-Henke, D. Kuai, M. Gerasimov, F. Roder, P. B. Balbuena and U. Krewer, *Nat. Commun.*, 2023, **14**, 6823.
29. P. Guan, L. Liu and X. Lin, *Journal of The Electrochemical Society*, 2015, **162**, A1798-A1808.
30. S.-H. Lee, H.-G. You, K.-S. Han, J. Kim, I.-H. Jung and J.-H. Song, *Journal of Power Sources*, 2014, **247**, 307-313.

View Article Online
DOI: 10.1039/D5EE01030F

31. E. W. C. Spotte-Smith, R. L. Kam, D. Barter, X. Xie, T. Hou, S. Dwaraknath, S. M. Blau and K. A. Persson, *ACS Energy Letters*, 2022, **7**, 1446-1453.
32. L. Chen, H. W. Zhang, L. Y. Liang, Z. Liu, Y. Qi, P. Lu, J. Chen and L.-Q. Chen, *Journal of Power Sources*, 2015, **300**, 376-385.
33. L. Liang and L.-Q. Chen, *Applied Physics Letters*, 2014, **105**.
34. L. Liang, Y. Qi, F. Xue, S. Bhattacharya, S. J. Harris and L.-Q. Chen, *Phys. Rev. E.*, 2012, **86**, 51609-51609.
35. Z. Liu, Y. Li, Y. Ji, Q. Zhang, X. Xiao, Y. Yao, L.-Q. Chen and Y. Qi, *Cell Reports Physical Science*, 2021, **2**, 100294-100294.
36. H. K. Tian, Z. Liu, Y. Ji, L.-Q. Chen and Y. Qi, *Chemistry of Materials*, 2019, **31**, 7351-7359.
37. Q. Wang, G. Zhang, Y. Li, Z. Hong, D. Wang and S. Shi, *npj Computational Materials*, 2020, **6**, 1-8.
38. D. Cao, K. Zhang, W. Li, Y. Zhang, T. Ji, X. Zhao, E. Cakmak, J. Zhu, Y. Cao and H. Zhu, *Advanced Functional Materials*, 2023, **33**.
39. W. Mu, X. Liu, Z. Wen and L. Liu, *Journal of Energy Storage*, 2019, **26**, 100921-100921.
40. V. Yurkiv, T. Foroozan, A. Ramasubramanian, R. Shahbazian-Yassar and F. Mashayek, *Electrochimica Acta*, 2018, **265**, 609-619.
41. J. Deng, G. J. Wagner and R. P. Muller, *Journal of The Electrochemical Society*, 2013, **160**, A487-A496.
42. P. Guan, X. Lin and L. Liu, *ECS Transactions*, 2014, **61**, 29-41.
43. Z. Gao, Y. Bai, H. Fu, J. Yang, T. Ferber, J. Feng, W. Jaegermann and Y. Huang, *Advanced Functional Materials*, 2022, **32**, 1-12.
44. R. A. Marcus, *Reviews of Modern Physics*, 1993, **65**, 599-610.
45. T. P. Silverstein, *Journal of Chemical Education*, 2012, **89**, 1159-1167.
46. J. Wagner-Henke, D. Kuai, M. Gerasimov, F. Roder, P. B. Balbuena and U. Krewer, *Nat Commun*, 2023, **14**, 6823.
47. J. W. Abbott and F. Hanke, *J Chem Theory Comput*, 2022, **18**, 925-934.
48. A. L. Michan, M. Leskes and C. P. Grey, *Chemistry of Materials*, 2015, **28**, 385-398.
49. D. Bedrov, O. Borodin and J. B. Hooper, *The Journal of Physical Chemistry C*, 2017, **121**, 16098-16109.
50. A. Wang, S. Kadam, H. Li, S. Shi and Y. Qi, *npj Computational Materials*, 2018, **4**.
51. Q. Wu, M. T. McDowell and Y. Qi, *J Am Chem Soc*, 2023, **145**, 2473-2484.
52. Y. X. Lin, Z. Liu, K. Leung, L.-Q. Chen, P. Lu and Y. Qi, *Journal of Power Sources*, 2016, **309**, 221-230.
53. F. A. Soto, Y. Ma, J. M. Martinez de la Hoz, J. M. Seminario and P. B. Balbuena, *Chemistry of Materials*, 2015, **27**, 7990-8000.
54. L. Dong, H. J. Yan, Q. X. Liu, J. Y. Liang, J. Yue, M. Niu, X. Chen, E. Wang, S. Xin, X. Zhang, C. Yang and Y. G. Guo, *Angew Chem Int Ed Engl*, 2024, **63**, e202411029.
55. F. Joho, B. Rykart, A. Blome, P. Novák, H. Wilhelm and M. E. Spahr, *Journal of Power Sources*, 2001, **97-98**, 78-82.
56. M. Yu, K. Liu, M. Li, J. Yan, C. Cao, J. Tan, J. Liang, K. Guo, W. Cao, P. Lan, Q. Zhang, Y. Zhou and P. Lu, *Light Sci. Appl.*, 2022, **11**, 215.
57. S. Menkin, C. A. O'Keefe, A. B. Gunnarsdottir, S. Dey, F. M. Pesci, Z. Shen, A. Aguadero and C. P. Grey, *Journal of Physical Chemistry C: Nanomaterials and interfaces*, 2021, **125**, 16719-16732.
58. X. He, D. Bresser, S. Passerini, F. Baakes, U. Krewer, J. Lopez, C. T. Mallia, Y. Shao-Horn, I. Cekic-Laskovic, S. Wiemers-Meyer, F. A. Soto, V. Ponce, J. M. Seminario, P. B. Balbuena, H. Jia, W. Xu, Y. Xu, C. Wang, B. Horstmann, R. Amine, C.-C. Su, J. Shi, K. Amine, M. Winter, A. Latz and R. Kostecki, *Nature Reviews Materials*, 2021, **6**, 1036-1052.
59. D. Aurbach, *Journal of Power Sources*, 2000, **89**, 206-218.

View Article Online
DOI: 10.1039/D5EE01030F

60. D. M. Seo, D. Chalasani, B. S. Parimalam, R. Kadam, M. Nie and B. L. Lucht, *ECS Electrochemistry Letters*, 2014, **3**, A91-A93.
61. S. K. Heiskanen, J. Kim and B. L. Lucht, *Joule*, 2019, **3**, 2322-2333.
62. G. M. Hobold, A. Khurram and B. M. Gallant, *Chemistry of Materials*, 2020, **32**, 2341-2352.
63. B. von Holtum, C. Peschel, U. Rodehorst, D. Wang, Y. Shao-Horn, M. Winter, S. Nowak and S. Wiemers-Meyer, *Journal of The Electrochemical Society*, 2025, **172**.
64. Z. Liu, P. Lu, Q. Zhang, X. Xiao, Y. Qi and L.-Q. Chen, *Journal of Physical Chemistry Letters*, 2018, **9**, 5508-5514.
65. J. M. Garcia-Lastra, J. S. G. Myrdal, R. Christensen, K. S. Thygesen and T. Vegge, *The Journal of Physical Chemistry C*, 2013, **117**, 5568-5577.
66. S. Shi, Y. Qi, H. Li and L. G. Hector, *The Journal of Physical Chemistry C*, 2013, **117**, 8579-8593.
67. M. Feng, J. Pan and Y. Qi, *Journal of Physical Chemistry C*, 2021, **125**, 15821-15829.
68. M. Smeu and K. Leung, *Phys Chem Chem Phys*, 2021, **23**, 3214-3218.
69. S. Shi, P. Lu, Z. Liu, Y. Qi, L. G. Hector, H. Li and S. J. Harris, *Journal of the American Chemical Society*, 2012, **134**, 15476-15487.
70. J. Heine, P. Hilbig, X. Qi, P. Niehoff, M. Winter and P. Bieker, *Journal of The Electrochemical Society*, 2015, **162**, A1094-A1101.
71. S. Singsen, F. Ospina-Acevedo, S. Suthirakun, P. Hirunsit and P. B. Balbuena, *Phys Chem Chem Phys*, 2023, **25**, 26316-26326.
72. Y. Ji and L. Q. Chen, *Acta Materialia*, 2022, **234**, 118007-118007.
73. K. Tasaki, z. A. Goldberg, J.-J. Lian, M. Walker, A. Timmons and S. J. Harrisc, *Journal of The Electrochemical Society*, 2009, **156**, A1019-A1027.
74. K. Tasaki and S. J. Harris, *The Journal of Physical Chemistry C*, 2010, **114**, 8076–8083.
75. H. B. Akkerman, R. C. Naber, B. Jongbloed, P. A. van Hal, P. W. Blom, D. M. de Leeuw and B. de Boer, *Proc Natl Acad Sci U S A*, 2007, **104**, 11161-11166.
76. Z. Wang, D. L. Danilov, R. A. Eichel and P. H. L. Notten, *Journal of Power Sources Advances*, 2024, **29**.
77. B. Tjaden, D. J. L. Brett and P. R. Shearing, *International Materials Reviews*, 2018, **63**, 47-67.
78. S. J. An, J. Li, C. Daniel, D. Mohanty, S. Nagpure and D. L. Wood, *Carbon*, 2016, **105**, 52-76.
79. M. Esmaeilpour, S. Jana, H. Li, M. Soleymanibrojeni and W. Wenzel, *Advanced Energy Materials*, 2023, **13**.
80. M. J. Frisch, G. W. Trucks, H. B. Schlegel, G. E. Scuseria, M. A. Robb, J. R. Cheeseman, G. Scalmani, V. Barone, G. A. Petersson, H. Nakatsuji, X. Li, M. Caricato, A. Marenich, J. Bloino, B. G. Janesko, R. Gomperts, B. Mennucci, H. P. Hratchian, J. V. Ort and D. J. Fox, *Journal*, 2016.
81. Y. Zhao and D. G. Truhlar, *Theoretical Chemistry Accounts*, 2008, **120**, 215-241.
82. S. Debnath, V. A. Neufeld, L. D. Jacobson, B. Rudshteyn, J. L. Weber, T. C. Berkelbach and R. A. Friesner, *The Journal of Physical Chemistry A*, 2023, **127**, 9178-9184.
83. H. Neugebauer, F. Bohle, M. Bursch, A. Hansen and S. Grimme, *The Journal of Physical Chemistry A*, 2020, **124**, 7166-7176.
84. D. Coskun, S. V. Jerome and R. A. Friesner, *Journal of Chemical Theory and Computation*, 2016, **12**, 1121-1128.
85. S. Grimme, S. Ehrlich and L. Goerigk, *Journal of Computational Chemistry*, 2011, **32**, 1456-1465.
86. A. V. Marenich, C. J. Cramer and D. G. Truhlar, *Journal of Physical Chemistry B*, 2009, **113**, 6378-6396.
87. O. Borodin, W. Behl and T. R. Jow, *Journal of Physical Chemistry C*, 2013, **117**, 8661-8682.
88. D. S. Hall, J. Self and J. R. Dahn, *Journal of Physical Chemistry C*, 2015, **119**, 22322-22330.
89. R. A. Marcus, *The Journal of Chemical Physics*, 1965, **43**, 679-701.

View Article Online
DOI: 10.1039/D5EE01030F

90. S. F. Nelsen, S. C. Blackstock and Y. Kim, *Journal of the American Chemical Society*, 1987, **109**, 677-682.
91. R. L. C. Akkermans, N. A. Spenley and S. H. Robertson, *Molecular Simulation*, 2021, **47**, 540-551.
92. X. He, Y. Zhu, A. Epstein and Y. Mo, *npj Computational Materials*, 2018, **4**.

View Article Online
DOI: 10.1039/D5EE01030F

Data Availability Statement

The first-principles computational results on the structure of reaction products and the COMSOL input file for this model are available in the NOMAD repository at https://nomad-lab.eu/prod/v1/gui/user/uploads/upload/id/I6rPnwjtTAOafwYpwN_qPQ